Nano-Micro Letters

e-ISSN 2150-5551
CN 31-2103/TB

ARTICLE

https://doi.org/10.1007/s40820-023-01172-9

Cite as
Nano-Micro Lett.
(2023) 15:195

Received: 8 May 2023
Accepted: 15 July 2023

Competitive Redox Chemistries in Vanadium Niobium Oxide for Ultrafast and Durable Lithium Storage

Xiaobo Ding[1], Jianhao Lin[1], Huiying Huang[1], Bote Zhao[1], Xunhui Xiong[1] ✉

HIGHLIGHTS

- The over-reduction from Nb^{5+} to Nb^{3+} in the lithiation process have been demonstrated to be the critical reason for the capacity decay of Nb_2O_5 for the first time.
- A novel competitive redox strategy has been proposed to suppress the over-reduction of Nb^{5+} to Nb^{3+}, which can be achieved by the incorporation of vanadium to form a new rutile $VNbO_4$ anode.
- The performance of $VNbO_4$ anode designed in this study stands among the best in cycle stability.

ABSTRACT Niobium pentoxide (Nb_2O_5) anodes have gained increasing attentions for high-power lithium-ion batteries owing to the outstanding rate capability and high safety. However, Nb_2O_5 anode suffers poor cycle stability even after modified and the unrevealed mechanisms have restricted the practical applications. Herein, the over-reduction of Nb^{5+} has been demonstrated to be the critical reason for the capacity loss for the first time. Besides, an effective competitive redox strategy has been developed to solve the rapid capacity decay of Nb_2O_5, which can be achieved by the incorporation of vanadium to form a new rutile $VNbO_4$ anode. The highly reversible V^{3+}/V^{2+} redox couple in $VNbO_4$ can effectively inhibit the over-reduction of Nb^{5+}. Besides, the electron migration from V^{3+} to Nb^{5+} can greatly increase the intrinsic electronic conductivity for $VNbO_4$. As a result, $VNbO_4$ anode delivers a high capacity of 206.1 mAh g^{-1} at 0.1 A g^{-1}, as well as remarkable cycle performance with a retention of 93.4% after 2000 cycles at 1.0 A g^{-1}. In addition, the assembled lithium-ion capacitor demonstrates a high energy density of 44 Wh kg^{-1} at 5.8 kW kg^{-1}. In summary, our work provides a new insight into the design of ultra-fast and durable anodes.

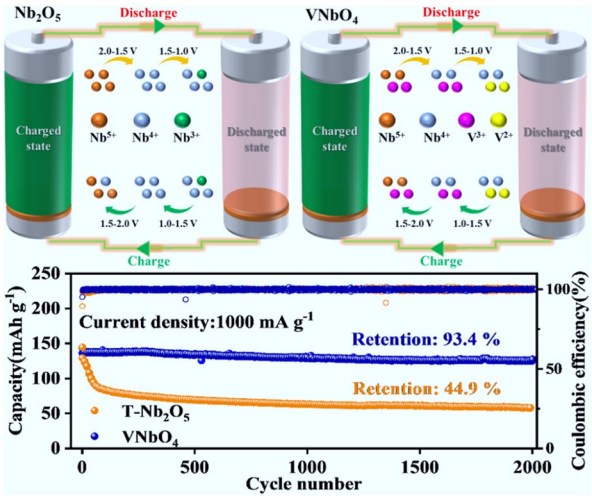

KEYWORDS Niobium pentoxide; Capacity decay; Over-reduction; Vanadium niobium oxide; Lithium-ion capacitor

✉ Xunhui Xiong, esxxiong@scut.edu.cn
[1] School of Environment and Energy, Guangdong Provincial Key Laboratory of Advanced Energy Storage Materials, South China University of Technology, Guangzhou 510640, People's Republic of China

Published online: 10 August 2023

1 Introduction

With the explosive growth of electric vehicles in the recent years, the inadequate power density and safety concerns have become the pivotal challenges of lithium-ion batteries (LIBs) and sodium-ion batteries (SIBs) for their further developments [1, 2]. However, the state-of-the-art graphite-based anodes cannot meet these critical demands because the low working potentials at 0.2 V can easily result in the generation of Li dendrites at high charge current densities [3–5]. In addition, the formation of a thick SEI film on surface of graphite anode at such low potential window hinders the fast transport of Li ions and increases heat amount, which will accelerate the deterioration of battery performance [6]. Thereafter, $Li_4Ti_5O_{12}$ (LTO) and TiO_2(B) anodes have been widely investigated as fast-charging electrodes owing to their fast Li^+ insertion mechanism at ~ 1.55 V (vs. Li^+/Li) [7, 8]. However, the rather low specific capacities severely restrict the applications in high-energy–density LIBs. Compared with Ti-based oxides, Nb_2O_5 shows a higher theoretical capacity owing to the rich redox chemistry of Nb element (Nb^{5+}/Nb^{4+}, Nb^{4+}/Nb^{3+}) in the potential range between 1.0 and 3.0 V versus Li^+/Li as well as superior rate performances [9]. Besides, the electrolyte decomposition and the Li dendrite formation at anode side can be prevented, leading to a high safety for the Nb_2O_5-based batteries [10]. It is worth noting that the Nb_2O_5 exists in different polymorphs, including pseudohexagonal Nb_2O_5 (TT-Nb_2O_5), orthorhombic Nb_2O_5 (T-Nb_2O_5), tetragonal Nb_2O_5 (M-Nb_2O_5), and monoclinic Nb_2O_5 (H-Nb_2O_5), which show greatly different Li storage performances [11]. T-Nb_2O_5 possesses alternating loosely packed 4 g atomic layers and densely packed 4 h atomic layers in the *c*-axis direction, in which 4 g layer provides the space of inserted Li^+ and 4 h layer provides coordination oxygen for Li^+ diffusion with low steric hindrance, leading to excellent rate performances, while H-Nb_2O_5 with the Wadsley–Roth shear phase shows a flat potential plateau at ~ 1.65 V (vs. Li^+/Li) owing to the two-phase transition process during the charge/discharge processes [12, 13]. Nevertheless, the poor electronic conductivity significantly restricts the applications of all the Nb_2O_5-based anodes for high-power LIBs [14].

Recently, various strategies have been developed to improve the rate performances of Nb_2O_5, including designing different Nb_2O_5 nanostructures, heteroatom doping and composing carbon matrix [15–17]. For example, Nb_2O_5 nanorod film grown directly on flexible carbon cloth showed a high Li storage capacity of 220 mAh g^{-1} at 0.5C and 160.6 mAh g^{-1} at 20C, respectively, which can be attributed to the remarkably decreased transfer distances of Li^+/electrons in the charge–discharge processes [18]. *N* doping can greatly improve the electronic/ionic conductivities of Nb_2O_5, thus it exhibits high capacities of 202.9 and 104.6 mAh g^{-1} at current densities of 0.1C and 25C, respectively [19]. T-Nb_2O_5-carbon-graphene composite delivered a high capacity of 206 mAh g^{-1} at 0.5C and 114 mAh g^{-1} at 100C [20]. Despite of these impressive progresses in enhancing rate performances, almost all of the Nb_2O_5 anodes still showed fast capacity decay (Table S1), which has not yet been overcome in the previous works and the mechanisms are remaining unclear. For example, S-doped T-Nb_2O_5 encapsulated into S-doped graphene (S-Nb_2O_5@S-rGO) demonstrated a poor cycle stability from 325 to 215 mAh g^{-1} after 100 cycles at 0.5C [21]. Similar phenomenon is also observed in Nb_2O_{5-x} NP, which showed fast capacity deterioration from 245 to 175 mAh g^{-1} after 200 cycles at 0.2 A g^{-1} [22]. Therefore, the in-depth investigation of the fast capacity decay during the long-term cycles and the exploration of efficient strategies to address this challenge are urgently needed.

Herein, the over-reduction of Nb^{5+} into Nb^{3+} in the lithiation process and then the incomplete oxidation in the following delithiation process have been demonstrated to be the critical reason for the rapid capacity decrease in Nb_2O_5 during cycling. Based on the failure mechanism, vanadium has been proposed to incorporate into Nb_2O_5 to form a new rutile $VNbO_4$ anode. Experimental data and theoretical calculation results indicate that the redox reaction of V^{3+}/V^{2+} couple has remarkable priority over Nb^{4+}/Nb^{3+} couple in the potential range of 1.0–1.5 V due to the stronger chemical affinity between Li and V atoms. Therefore, V^{3+}/V^{2+} redox couple can effectively inhibit the irreversible over-reduction of Nb^{5+} to Nb^{3+}, thus avoiding the rapid capacity decay in the long-term cycles. In addition, the electron migration from V^{3+} to Nb^{5+} leads to a superior intrinsic electronic conductivity for $VNbO_4$. The significant enhancement of electronic conductivity and the reversibility of the redox

https://doi.org/10.1007/s40820-023-01172-9

reaction during charge/discharge processes endows $VNbO_4$ electrode with fast and durable Li storage performances.

2 Experimental and Methods

2.1 Materials Synthesis

Firstly, 0.001 mol niobium chloride ($NbCl_5$, 99.9%, Macklin) and 0.001 mol vanadium (III) 2,4-pentanedionate ($C_{15}H_{21}O_6V$, 99.9%, Macklin) were added to the mixed solution of 35 mL ethanol and 5 mL deionized water to form a suspension. Then, added 0.6 g urea (CH_4N_2O, 99.9%, Macklin), 0.63 g oxalic acid ($C_2H_2O_4$, 99.5%, Macklin) and 0.063 g F127 (99.9%, Sigma-Aldrich) under vigorous stirring, kept stirring at room temperature for 30 min until the solution became clear. The obtained green transparent solution was transferred to a 100 mL Teflon autoclave and reacted at 180 °C for 18 h. After cooling to room temperature, the mixture was filtered and washed with ethanol (C_2H_5OH, 99.9%, Damao chemical reagent factory) for 5 times, and put into a vacuum drying oven for overnight drying. After that, the obtained precursor was transferred to corundum crucible, kept at 600 °C for 3 h in Ar protected tubular furnace, and then cooled naturally to obtain black $VNbO_4$ powder. For comparison, T-Nb_2O_5 was also prepared via same synthesis process without V source.

2.2 Materials Characterizations

The phase and structure of the samples were analyzed by X-ray diffraction analyzer (XRD, Bruker D8 advanced, Cu, K) α, $\lambda = 1.5418$ Å), the finer crystal structure parameters are obtained by Rietveld refinement method. The micro-morphology of the samples was obtained by cold field emission electron microscope (SEM, Hitachi SU8010). The internal structure, lattice arrangement and element distribution of the material were detected by field emission transmission electron microscope (TEM, JEOL, 3200Fs, accelerating voltage = 300 kV). The valence states of the elements in the samples were obtained by X-ray photoelectron spectroscopy (XPS, Thermo ESCALAB 250XI. The electronic conductivity was collected by the four-probe powder resistivity tester (ST2722-sd). UV–*vis* spectra were obtained by PE lambda 750. BET specific surfaces were collected by JW-BK200C surface area and pore size analyzer (Beijing JWGB Sci. & Tech. Co., Ltd) at the liquid-nitrogen boiling point (77 K).

In situ XRD testing is based on a self-made in situ testing system. The LIB-XRD *in situ* cell module (Beijing Scistar Technology Co., Ltd.) was assembled by anode of carbon paper loaded with active substances and cathode of Li metal foil; while, Be foil is installed on the top of the in situ battery as a window for X-ray. In the initial charge discharge test, XRD diffraction spectra were continuously collected 2θ (degree) range of 10°–55° with step increment of 0.02° at a scanning rate of 0.06° s^{-1}.

2.3 Electrochemical Measurements

The electrode preparation process is as follows: Active materials, acetylene black (Guangdong Canrd New Energy Technology Co., Ltd.) and polytetrafluoroethylene (PVDF, Mw = 400,000, Macklin) were mixed with the ratio of 8:1:1. The slurry was obtained after added drops *N*-methyl-2-pyrrolidone (NMP, 99.5%, Macklin) and then coated on one side of copper foil. After drying for 12 h in 80 °C, the copper foil was punched as disc with a diameter of 13 mm. The mass of materials loading on each disc was about 1.3–1.4 mg. The CR2032 coin type cells were assembled in a glovebox and each cell was composed of the above electrode, separator (polyethylene membrane, Celgard), counter electrode (lithium tablet, China Energy Lithium Co., Ltd.) and electrolyte (1.0 M $LiPF_6$ in EC: DMC: EMC = 1:1:1 vol%, www.dodochem.com). The LAND2001CT battery testing system was employed for galvanostatic charging/discharging measurements. And a constant temperature drying oven at 60 °C and a constant temperature refrigerator at − 10 °C were used as battery test boxes for electrochemical test in a wide temperature range.

The assembly process of full cell is the same as above, while replaced lithium foil with commercial cathode ($LiFePO_4$@C: acetylene black: PVDF = 8:1:1) as counter electrode.

The assembly process of lithium-ion capacitor is the same as above, while replaced lithium foil with active carbon electrode (active carbon: acetylene black: PVDF = 8:1:1) as counter electrode.

The cyclic voltammetry (CV) test at a voltage range of 1.0–3.0 V and EIS test with a frequency range of 100,000–0.01 HZ was carried on a electrochemical workstation (CHI660E, Chenhua, Shanghai).

The energy/power density of lithium-ion capacitor can be obtained by Eqs. (1) and (2):

$$E = \int_{t1}^{t2} IV(t)dt \quad (1)$$

$$P = \frac{E}{t} \quad (2)$$

where I (A g^{-1}) is the constant current density based on the total active materials, V (V) is the working voltage, $t1$ and $t2$ is the discharge start/end time (s), and t (s) is the discharging time of lithium-ion capacitor. E is the energy density and P is the power density.

2.4 Density Functional Theory Calculation Method

All the calculations for structure optimization have been carried out with the Vienna Ab Initio Simulation Package (VASP) at the density functional theory (DFT) based with 3D periodic conditions. The exchange–correlation functional was treated by generalized gradient approximation (GGA) with the Perdew–Burke–Ernzerhof (PBE). The electron–ion interaction was treated by the projector-augmented wave method (PAW) that the core electrons were treated with cost-effective pseudopotentials implemented in VASP, and the valence electrons were expanded by plane-wave basis with the kinetic cutoff energy of 520 eV. The electronic energy was considered self-consistent when the energy change was smaller than 10^{-5} eV with a $4 \times 1 \times 3$ Monkhorst–Pack k-point grid for Brillouin zone sampling. Grimme's DFT-D3 methodology was used to describe the dispersion interactions. In addition, since the number and species of each atom are the same, we judge the trend based on the total energy of the model of the four sites where Li ions are inserted.

3 Results and Discussion

3.1 Physical Characterization Results

The $VNbO_4$ was prepared by a facile surfactant-assisted hydrothermal treatment of the mixed solution of $NbCl_5$ and $C_{15}H_{21}O_6V$ with stoichiometric ratio followed by an annealing process in Ar flow, as shown in Fig. 1a. For comparison, T-Nb_2O_5 was also prepared via the same synthesis process without V source. The XRD spectra in Fig. 1b show the structural information of the as-prepared $VNbO_4$ and T-Nb_2O_5. The diffraction peaks of $VNbO_4$ at 26.9°, 35.3° and 39.2° correspond to (110), (101) and (220) planes, while the diffraction peaks of T-Nb_2O_5 at 22.5°, 28.5° and 36.7° correspond to (001), (180) and (200) planes, both of them being consistent with the previous reports [9, 23]. To understand the structure advantages of $VNbO_4$ as electrode material, Rietveld refinement was employed to analyze the XRD pattern of $VNbO_4$, as shown in Fig. 1c (Rietveld refinement pattern of T-Nb_2O_5 is exhibited in Fig. S1). The results show that $VNbO_4$ belongs to rutile structure with *P42/mnm* space group (a, $b = 4.6956$ Å, $c = 3.0336$ Å, $\alpha = \beta = \gamma = 90°$). The corresponding crystal model in Fig. 1d clearly shows that the open tunnel in the c-axis direction provides the efficient Li^+ insertion site and transport channel.

Except for different crystal structure, the core-level Nb 3*d* XPS spectra reveal the different Nb valence states in T-Nb_2O_5 and $VNbO_4$. As shown in Figs. S2 and 1e, the typical double peaks of Nb $3d_{3/2}$ and Nb $3d_{5/2}$ formed by the spin–orbit splitting are located at 210.1 and 207.4 eV in T-Nb_2O_5, which indicates that Nb element is existed in the highest oxidation state (Nb^{5+}) [24]. In the $VNbO_4$, Nb $3d_{3/2}$ and Nb $3d_{5/2}$ peaks are located at obviously lower binding energies of 209.6 and 206.8 eV, respectively, which demonstrates that the valence-shell electron state of Nb atoms in $VNbO_4$ is different from that in T-Nb_2O_5. To further reveal the changed electron clouds of metal elements in $VNbO_4$, the V 2*p* XPS spectrum is shown in Fig. S3. Two characteristic peaks of V^{3+} are located at 524.1 and 517.2 eV, respectively, which are higher than the typical binding energies in the previous reports [25, 26]. The abnormal binding energies of Nb 3*d* and V 2*p* XPS spectra can be attributed to the valence-shell electron migration from V^{3+} to Nb^{5+}, in which V^{3+} serves as an electron donor due to its reduction ability and Nb^{5+} as an electron acceptor due to its oxidation ability. UV–vis tests were carried out to verify the influence of electron clouds transfer from V to Nb on the electronic conductivity. As displayed in Fig. 1f, the band gap of $VNbO_4$ (3.13 eV) is obviously small than that of T-Nb_2O_5 (3.42 eV). Furthermore, four-probe method electronic conductivity tests were performed to obtain the detailed electronic conductivity. As shown in Fig. 1g, $VNbO_4$ exhibits

 https://doi.org/10.1007/s40820-023-01172-9

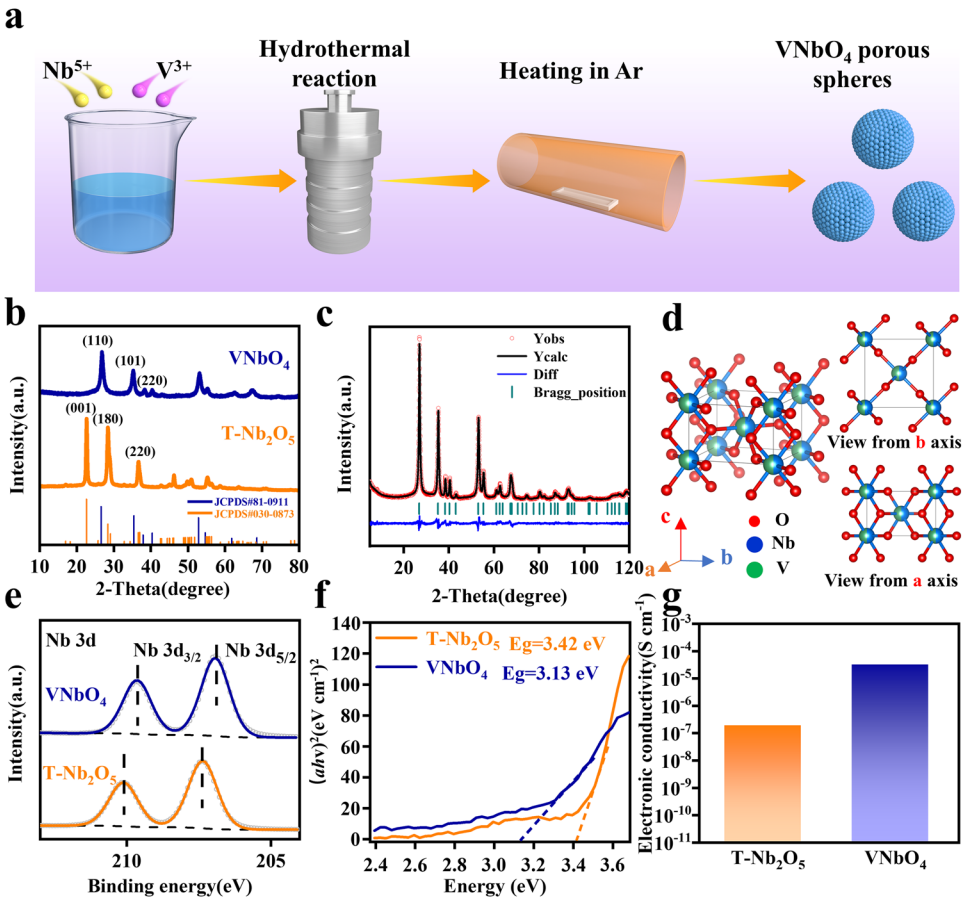

Fig. 1 **a** Synthesis strategy of $VNbO_4$. **b** XRD patterns of T-Nb_2O_5 and $VNbO_4$. **c** Rietveld refinement pattern of $VNbO_4$. **d** Crystal model of $VNbO_4$. **e** The high-resolution Nb 3*d* XPS spectra of T-Nb_2O_5 and $VNbO_4$. **f** Ultraviolet–visible spectroscopy and **g** the electronic conductivities of T-Nb_2O_5 and $VNbO_4$ measured by four-probe method

a high electronic conductivity of 3.11×10^{-5} S cm^{-1}, two orders higher than that of T-Nb_2O_5 (1.85×10^{-7} S cm^{-1}). Therefore, the spontaneous regulation of valence-shell electrons endows $VNbO_4$ with greatly enhanced electronic conductivity.

3.2 Morphological Characterization Results

The microstructures of $VNbO_4$ and T-Nb_2O_5 were investigated via SEM and TEM. As shown in Fig. 2a–d, both of two samples show spherical morphology with a diameter of 300–700 nm as well as uniformly distributed pores. Brunauer–Emmett–Teller (BET) method was employed to obtain detailed information on the pore structure of T-Nb_2O_5 and $VNbO_4$ (Fig. S2). The results show that both T-Nb_2O_5 and $VNbO_4$ have mesoporous structure with the pore volume of about 0.06 m^3 g^{-1} and the pore size of 3–20 nm. The BET results and TEM images in Figs. 2e and S4 illustrate that the pores on the surface are extended to the bulk, which can facilitate the full infiltration of electrolyte and provide buffer space for volume expansion of during the charge process [27]. High resolution TEM images show both T-Nb_2O_5 and $VNbO_4$ have high crystallinity (Figs. 2f–g and S5). The $VNbO_4$ exhibits two kinds of crystal plane spacing of 4.61 and 2.89 Å, which correspond to (110) and (101) planes of $VNbO_4$, respectively. The selected-area electron diffraction (SAED) pattern exhibited in Fig. 2h demonstrates that $VNbO_4$ possesses a polycrystalline structure with well-defined diffraction rings of (110), (101) and (211) planes. The element distribution of $VNbO_4$ can be characterized by the energy dispersive spectrometer (EDS). As shown in Fig. 2i–l, V, Nb and O elements are very evenly distributed in the whole spherical particle.

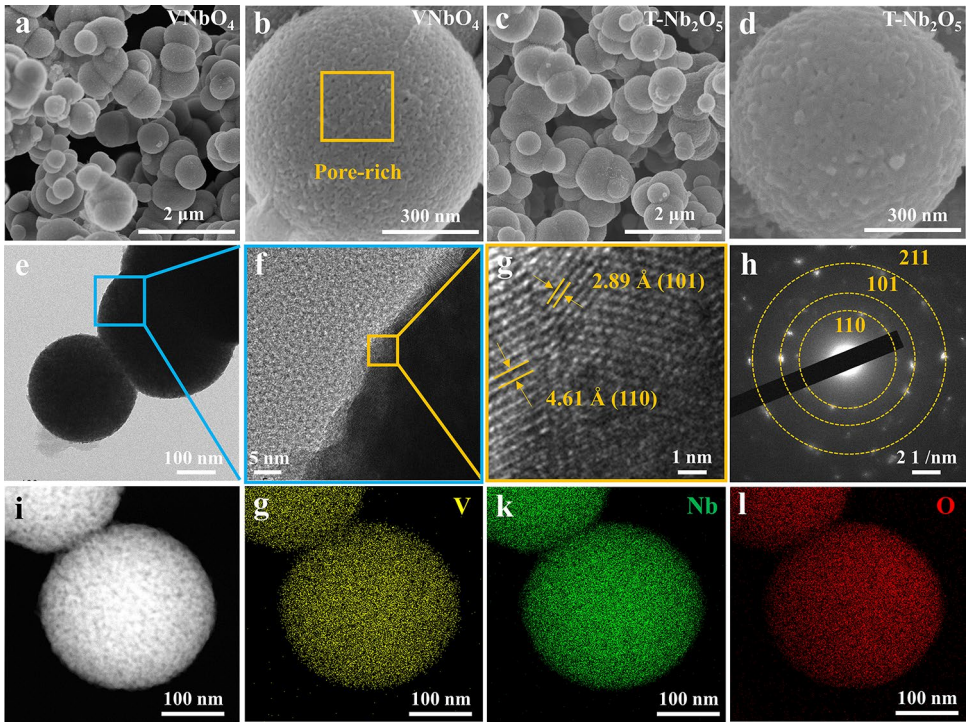

Fig. 2 SEM images of **a**, **b** $VNbO_4$ and **c**, **d** T-Nb_2O_5 at different magnifications. **e**, **f** TEM images, **g** HRTEM image and **h** SADE pattern of $VNbO_4$. **i–l** EDS elements mapping images of $VNbO_4$

3.3 Electrochemical Properties in Half-Cell Tests

Then, the Li storage performances of $VNbO_4$ were evaluated in half cell in the potential range of 1.0–3.0 V and made a comparison with those of T-Nb_2O_5. The Li storage mechanism of the $VNbO_4$ was firstly investigated by *in situ* XRD on a live, specially designed cell with $VNbO_4$ anode working at a current density of 0.1 A g^{-1}. As shown in Fig. S6, when the cell was discharged from open circuit voltage (OCV) to 1.0 V, the characteristic peaks of (110), (200), (211), (002) and (301) shift to the lower degrees, which is caused by the Li^+ insertion into host $VNbO_4$, as observed in other insertion-type anodes [28, 29]. During the following charge process from 1.0 to 3.0 V, a full positive shift can be observed for the main diffraction peaks of $VNbO_4$. Similarly with Nb_2O_5, $VNbO_4$ also possesses the reversible solid-solution-like Li storage behavior without phase transformation, which can be confirmed by the *ex situ* HRTEM images of $VNbO_4$ anode at different discharge/charge states (Fig. S7). However, $VNbO_4$ demonstrates the different redox chemistries from Nb_2O_5, as illustrated by the CV curves in Fig. 3a. Similar with the typical pseudocapacitive RuO_2 anode [30–32], T-Nb_2O_5 demonstrates the typical broad redox peaks in potential range of 1.3–2.1 V, which can be attributed to the stepwise redox process from Nb^{5+} to Nb^{4+} and then Nb^{3+} cause by the Li^+ insertion [33, 34]. However, the most obvious redox peaks for $VNbO_4$ are located at a low potential range of 1.0–1.5 V, which corresponds to the redox couple of V^{3+}/V^{2+}, The peak area contributed by Nb redox reaction in potential range of 1.3–2.1 V is significantly reduced, which indicates that the capacity contribution from the redox reaction of Nb is reduced [35]. Besides, the CV curves at different sweep rates shown in Fig. S8 demonstrate that $VNbO_4$ still shows intercalation pseudocapacitive charge-storage behavior. Meanwhile, the initial charge–discharge curves at 0.1 A g^{-1} show that $VNbO_4$ and T-Nb_2O_5 exhibit similar initial Coulombic efficiency of about 80% (Fig. 3b). The large capacity loss may be attributed to the Li^+ inserted the disordered defect area in the crystal, as well as the conductive carbon in the electrode [36, 37]. Specifically, $VNbO_4$ anode can deliver a high charge capacity 206.1 mAh g^{-1}, which is higher than T-Nb_2O_5 anode (179.1 mAh g^{-1}). Meanwhile, $VNbO_4$ anode shows a lower

 https://doi.org/10.1007/s40820-023-01172-9

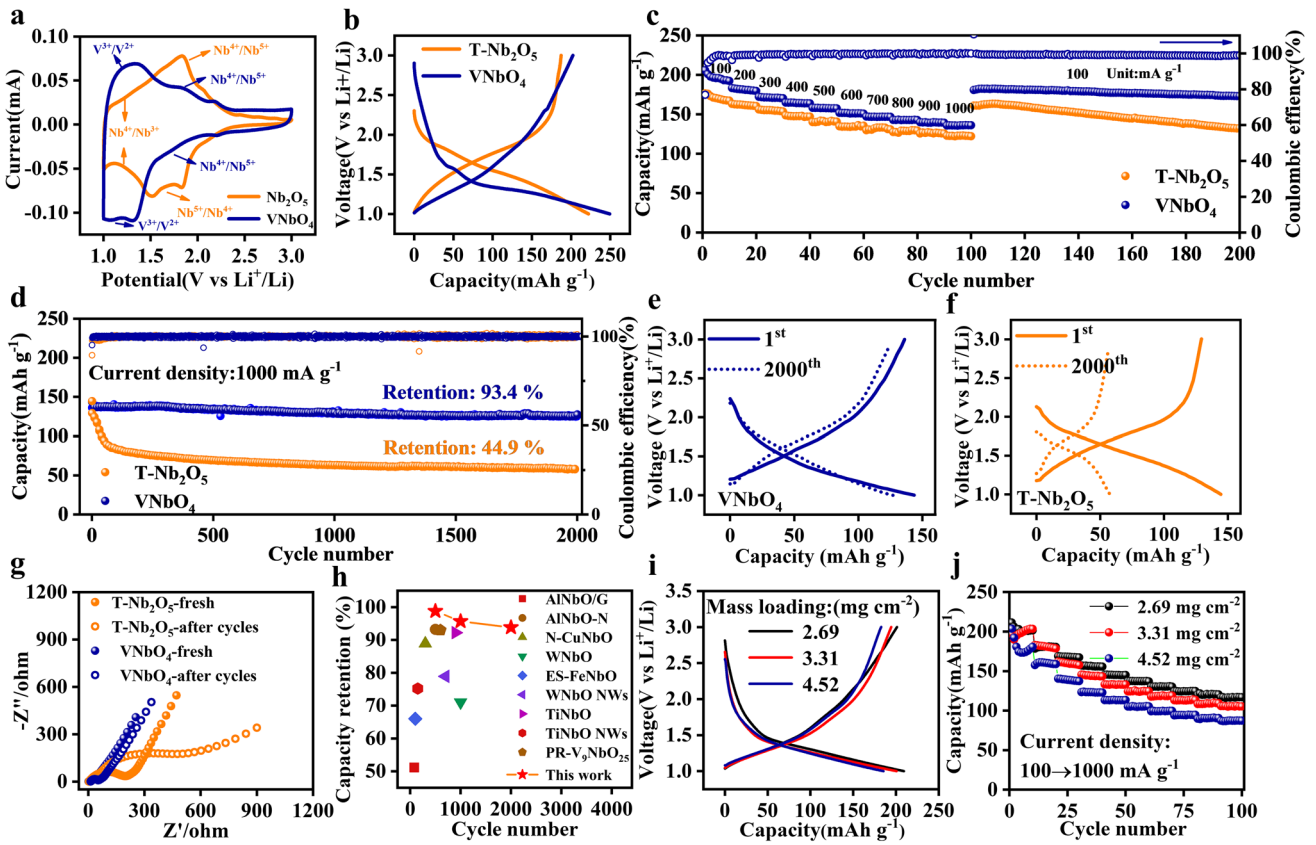

Fig. 3 **a** The initial CV curves at a sweep rate of 0.1 mV s^{-1}, **b** the initial charge–discharge profiles at 0.1 A g^{-1}, **c** the rate performances and the subsequent cycle performance at 100 mA g^{-1}, **d** the cycle performance at 1.0 A g^{-1} of $VNbO_4$ and T-Nb_2O_5 anodes. The selected charge–discharge profiles at 1.0 A g^{-1} of **e** $VNbO_4$ and **f** T-Nb_2O_5. **g** The AC impedance of two electrodes before and after 2000 cycles. **h** The comparison of cycle retention between $VNbO_4$ with previous works. **i** The charge–discharge profiles at 0.1 A g^{-1} and **j** the rate capacities of $VNbO_4$ with different mass loading

insertion/extraction Li plateau than T-Nb_2O_5, which agrees well with CV curve.

Besides, $VNbO_4$ also delivers improved rate performances with slight increase in potential polarization at various current densities, as displayed in Figs. 3c and S9. For example, $VNbO_4$ remains a remarkable capacity of 136.2 mAh g^{-1} at 1.0 A g^{-1}, while T-Nb_2O_5 only shows a capacity of 123.3 mAh g^{-1}. Noting that $VNbO_4$ can maintain a high retention ratio of 96.0% after 100 cycles when the current density was reset to 0.1 A g^{-1}, much higher than that of T-Nb_2O_5. The excellent cycle stability for $VNbO_4$ is also verified by the cycle performance at 1.0 A g^{-1}. As exhibited in Fig. 3d–e, $VNbO_4$ demonstrates an impressive capacity retention of 93.4% after 2000 cycles at high current density of 1.0 A g^{-1}, and the charge–discharge curve at 2000th cycle is well maintained. In sharp contrast, T-N_2O_5 experiences rapid capacity deterioration in the initial tens of cycles and a poor capacity retention of 44.9% is obtained after 2000 cycles with greatly increased polarization (Fig. 3f). Compared to the previous reported Nb-based bimetallic transition oxides ($AlNbO_4$/G [38], $AlNb_{11}O_{29}$-N [39], N-$Cu_2Nb_{34}O_{87}$ [40], $WNb_{12}O_{33}$ [24], ES-$FeNbO_4$ [41], $WNb_{12}O_{33}$ NWs [42], $TiNb_{24}O_{62}$ [43], $TiNb_6O_{17}$ NWs [44], PR-V_9NbO_{25} [45]), the performance of $VNbO_4$ anode designed in this study stands among the best in cycle stability, which can be also proved by the excellent electrochemical performances under high mass loading (Figs. 3g and S10) as well as at extreme temperatures (Fig. S11). At a loading of 4.52 mg cm^{-2}, a remarkable reversible capacity of 203.7 mAh g^{-1} is delivered at 0.1 A g^{-1} without obvious increased overpotential (Fig. 3h). Even at an elevated current density of 1.0 A g^{-1}, a capacity of 87.3 mAh g^{-1} can be still delivered (Fig. 3i).

To understand the different cycle stability between $VNbO_4$ and T-Nb_2O_5, the surface morphologies of two electrodes at different cycles were firstly characterized (Fig. S12). The SEM images of cycled $VNbO_4$ and T-N_2O_5 show that their sizes increase slightly without obvious pulverization after 500 and 2000 cycles, indicating that both of them have excellent structural stabilities during the repeated Li^+ insertion/extraction processes. Then the electrochemical impedance spectra (EIS) were conducted on electrodes with different cycle numbers (Fig. 3j). The charge transfer impedance (R_{ct}) of $VNbO_4$ electrode at initial state is obviously lower than T-N_2O_5 electrode, and experiences a slight increase after 2000 cycles (Fig. S13). In vast contrast, the R_{ct} of T-N_2O_5 electrode at 2000th cycle is significantly increased compared to the initial cycle. These results indicate that $VNbO_4$ can maintain good electron transfer in the whole electrochemical cycles.

3.4 Mechanism Discussion

Furthermore, e*ex situ* XPS was also carried out to analyze the valences of cation in both T-Nb_2O_5 and $VNbO_4$ at different lithiated/delithiated states in the initial charge–discharge process. For T-Nb_2O_5 at OCV state, the characteristic peaks of Nb 3*d* are located at 210.1 and 207.4 eV (Fig. 4a). After discharging to 1.5 V, the dominant peaks of Nb 3*d* shift to low binding energies of 208.2 and 205.4 eV, which represents that most Nb^{5+} is reduced to Nb^{4+}. The existence of weak doublet related to Nb^{5+} implies that the reduction reaction from Nb^{5+} to Nb^{4+} is not be completed at 1.5 V, and the characteristic peaks of Nb^{5+} are disappeared when discharged to 1.0 V. Meanwhile, a small doublet of Nb^{3+} can be observed at 207.4 and 204.9 eV, which suggests that partial Nb^{4+} is further reduced in the low potential range of 1.5–1.0 V. In the following delithiation process, the lithiation product Nb^{4+} is gradually converted into Nb^{5+}. However, Nb^{4+} is still observed even after a constant-potential charging process at 3.0 V for 30 min. Considering the Nb^{3+} will experience a two-step oxidation process to Nb^{5+} in the following delithiation process, the existence of Nb^{4+} in the full charged T-Nb_2O_5 state is largely attributed to the formation of Nb^{3+} in the lithiation process. Besides, the Nb 3*d* orbit XPS spectra of T-Nb_2O_5 electrode at different lithiated/delithiated states in the 50th and 100th charge–discharge process at 1 A g^{-1} strongly proves that Nb^{4+}/Nb^{3+}redox couple are not as reversible as Nb^{5+}/Nb^{4+} (Fig. S14). Therefore, the over-reduction of Nb^{5+} to Nb^{3+} should be main reason for the capacity loss for T-Nb_2O_5 anode. However, ex situ Nb 3*d* XPS spectra of $VNbO_4$ at different lithiated/delithiated states show remarkable differences. As shown in Fig. 4b, no Nb^{3+} is occurred in the voltage window of 1.0–1.5 V in the lithiation process and the Nb^{4+} can be completely converted into Nb^{5+} in the following delithiation process. Meanwhile, V^{3+} will be reduced to V^{2+} is in the voltage range of 1.0–1.5 V (Fig. 4c). Obviously, the redox couple of V^{3+}/V^{2+} has a higher priority over that of Nb^{4+}/Nb^{3+} couple in the range of 1.0–1.5 V. To provide more intuitive proof, the models of NbO_2 and V_2O_3 was created to calculate the energy barrier of Nb^{4+}/Nb^{3+} and V^{3+}/V^{2+}, as shown in Fig. S15. Through calculating the energy difference between the models before and after electron injection, it can be concluded that the energy barrier for V^{3+} to V^{2+} is 1.07 eV, which is significantly lower than the energy barrier for Nb^{4+} to Nb^{3+}(2.39 eV). Therefore, the reduction of V^{3+} in $VNbO_4$ takes priority over Nb^{4+} and can effectively suppress the generation of Nb^{3+} during the long-term cycling processes. Figure 4d shows the different redox chemistries in T-Nb_2O_5 and $VNbO_4$ during the electrochemical process. In the discharge process, some Nb^{5+} in T-Nb_2O_5 electrode will be over reduced to Nb^{3+}, and Nb will not return to the initial valence state in the following charge process. However, the introduction of V^{3+}/V^{2+} couple can effectively inhibit the over-reduction of Nb^{5+}. As a result, both Nb and V in $VNbO_4$ electrode exhibit highly reversible redox chemistries in the charge–discharge processes.

DFT calculation was employed to demonstrate the higher priority of V^{3+}/V^{2+} couple in the charge/discharge process via evaluating the affinity of V and Nb atoms to Li atoms. Four models with different Li insertion sites were created and the distance between Li and adjacent V atoms in each model and corresponding overall energy were calculated (Fig. 5a-d). The atomic distances of Li and V in four models are 3.165, 3.09, 3.01 and 3.015 Å, respectively (Table S2). The overall energy of each model is normalized based on the energy of model 1. The energy differences (ΔE) between model 2, 3 and 4 and model 1 are -0.19, -0.4 and -0.39 eV, respectively. Notice that the average distance between Li and V atom in model 3 is minimal, and the overall energy is the lowest (Fig. 5e), indicating that Li atoms are more inclined to choose the insertion site closer to V atom. Therefore, the highly reversible redox behavior of $VNbO_4$ can be attributed

 https://doi.org/10.1007/s40820-023-01172-9

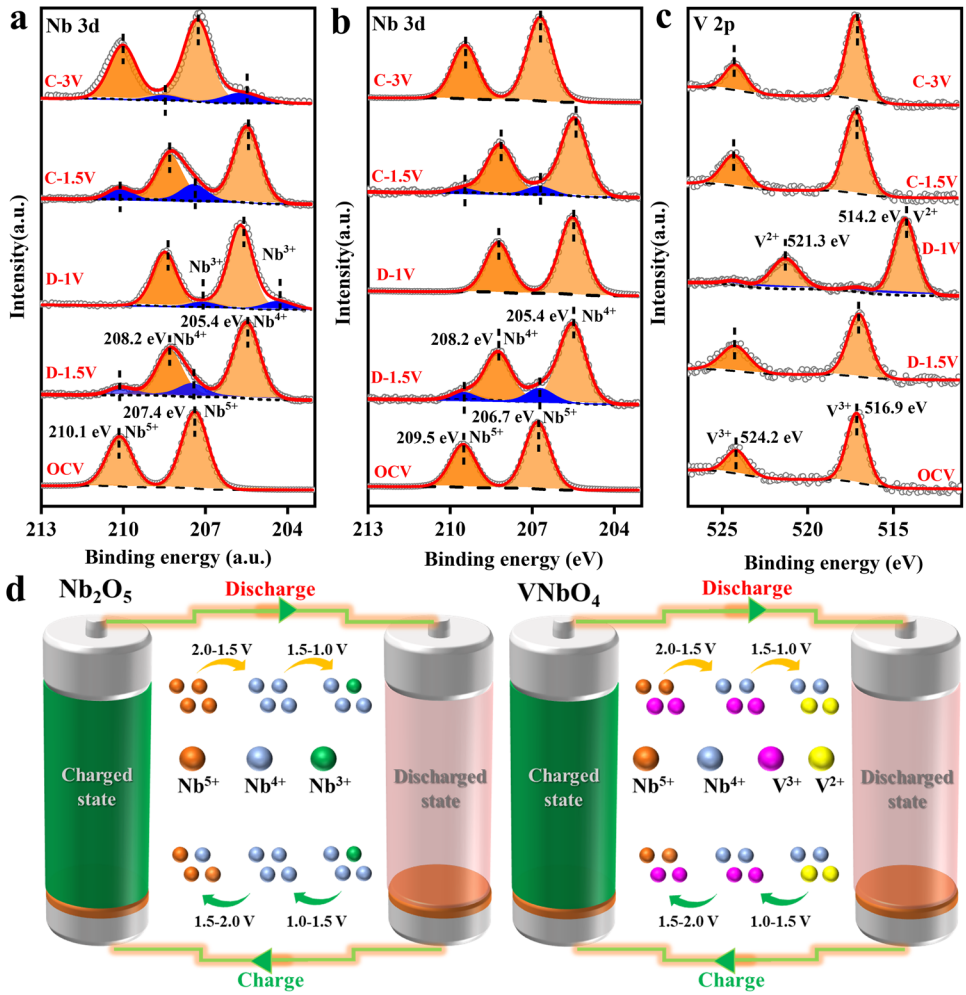

Fig. 4 *Ex situ* XPS spectra of **a** Nb 3*d* in T-Nb_2O_5, **b** Nb 3*d* and **c** V 2*p* in $VNbO_4$ anode at different lithiated/delithiated states. **d** Schematic diagram of redox chemistries in different anodes

to the competitive redox behavior caused by the introduction of V^{3+}/V^{2+} couple. In the potential range of 1.5 ~ 3.0 V, the redox conversion between Nb^{5+} and Nb^{4+} dominates the capacity contribution, while the redox reaction of V^{3+}/V^{2+} couple take priority over Nb^{4+}/Nb^{3+} couple in the potential range of 1.0 ~ 1.5 V owing to the stronger chemical affinity between Li atoms and V atoms. As results, $VNbO_4$ anode delivers excellent cycle stability via suppressing the over-reduction of Nb^{5+}.

To further demonstrate the conclusion, the post-mortem XPS analysis of $VNbO_4$ and T-Nb_2O_5 electrodes at fully charged state after 1000 cycles was carried out. As shown in Fig. 5f, a considerable amount of Nb in T-Nb_2O_5 cannot return to the initial Nb^{5+} state after long-term discharge–charge cycles, indicating that the irreversible redox chemistry of Nb is the main reason for the capacity decay. In sharp contrast, Nb^{5+} in $VNbO_4$ exhibits excellent reversibility after 1000 cycles (Fig. 5g). In addition, V also maintains a high reversibility in the long-term cycles (Fig. S16).

3.5 Electrochemical Properties in Practical Energy Storage Devices

Lastly, the potential of practical application for $VNbO_4$ anode was evaluated by assembling a full cell with commercial $LiFePO_4$@C cathode and a lithium-ion capacitor (LIC) with active carbon (AC) cathode, respectively (Fig. 6a). The electrochemical performances of $LiFePO_4$@C and AC in half cell (Li foil as counter electrodes) are shown in Figs. S17 and S18.

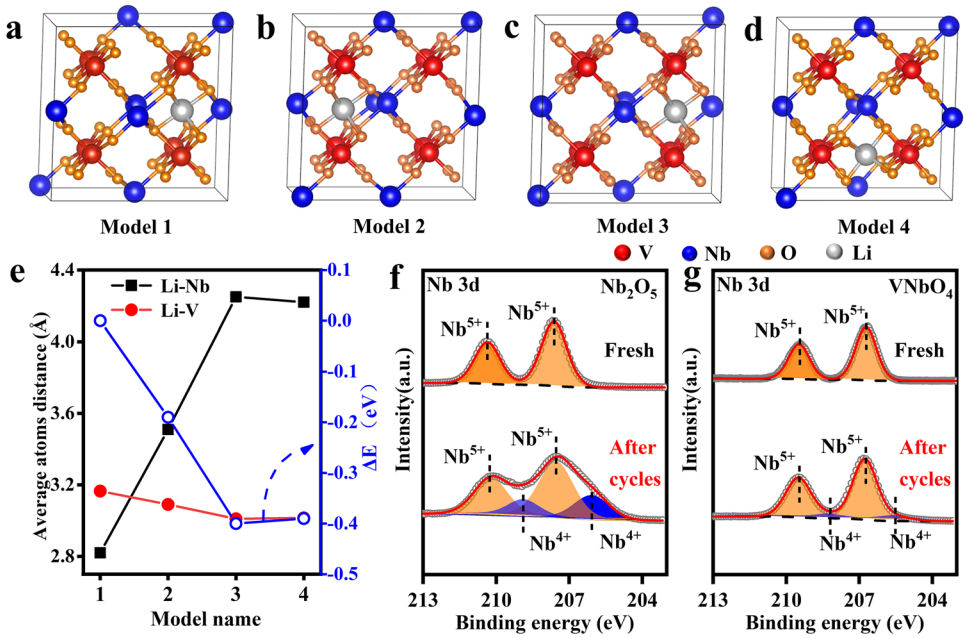

Fig. 5 **a–d** Crystal models of $VNbO_4$ with different lithium-insert sites. **e** Response of model energy to Li–Nb atomic distance or Li-V atomic distance. Nb 3*d* XPS spectra of **f** Nb_2O_5 and **g** $VNbO_4$ anode after 1000 cycles

The $LiFePO_4$@C//$VNbO_4$ full cell can deliver a discharge capacity of 122.6 mAh g^{-1} at 1C (1C = 170 mA g^{-1}) with an initial coulomb efficiency of 77.1% in potential range from 1.2 to 2.75 V (Fig. 6b). After 200 cycles at 1C, $LiFePO_4$@C//$VNbO_4$ remains a high discharge capacity of 97.8 mAh g^{-1} with a high retention of 79.8% (Fig. 6c). In a sharp contrast, $LiFePO_4$@C//T-Nb_2O_5 delivers a poor capacity of 45.5 mAh g^{-1} with retention of 38.5% after 190 cycles at 1C (Fig. S19). The full cell also demonstrates a superior rate performance with high capacities of 98.6, 83.1, 74.4, 63.7 mAh g^{-1} at 2C, 3C, 4C and 5C, respectively (Fig. 6d). The electrochemical performances of $VNbO_4$ anode in LIC were also studied in the potential range of 1.0–3.0 V. The overall mass loading of the two electrodes is about 4.5 mg cm^{-2}. Figure 6e shows the asymmetric CV curves of AC//$VNbO_4$ at different sweep rates of 5–100 mV s^{-1}, which exhibit a quasi-rectangular shape, illustrating that the fast physical adsorption/desorption of PF_6^- at the AC side and the relative sluggish intercalation/deintercalation kinetic of Li^+ at the $VNbO_4$ side are combined. In the following rate performance analysis (Fig. 6f-g), the LIC device can exhibit high capacitances of 103.3, 90.4, 87.9, 80.6, 72.1, 59.5 and 39.9 F g^{-1} at 0.05, 0.1, 0.2, 0.5, 1.0, 2.0 and 5.0 A g^{-1} respectively. As exhibited in Fig. 6h, the selected charge/discharge plots are highly overlapped, demonstrating the excellent reversibility of electrochemical behaviors of AC//$VNbO_4$. Thus, the LIC device constructed by AC cathode and $VNbO_4$ anode can deliver superior cycle stability with a retention of 67.5% after 5000 cycles (Fig. 6i). Ragone plot was obtained to clarify the relation of energy density and power density (Fig. 6j). AC//$VNbO_4$ can deliver a high energy density of 113 Wh kg^{-1} at 65 W kg^{-1} as well as an ultra-high power density of 5.8 kW kg^{-1} at 44 Wh kg^{-1}, which are much higher than many LICs previously reported [46–54]. In general, $VNbO_4$ shows excellent electrochemical performance in both LIB and LIC systems, which can be considered as a potential candidate of the next generation anode materials.

4 Conclusions

In this work, the over-reduction of Nb^{5+} in the lithiation process and the incomplete oxidation in the following delithiation process has been demonstrated to be a critical reason for the capacity decay of T-Nb_2O_5 for the first time. Then a competitive redox strategy has been proposed to suppress the over-reduction of Nb^{5+}, which has been achieved by the incorporation of vanadium to form a new rutile $VNbO_4$ anode. Due to

https://doi.org/10.1007/s40820-023-01172-9

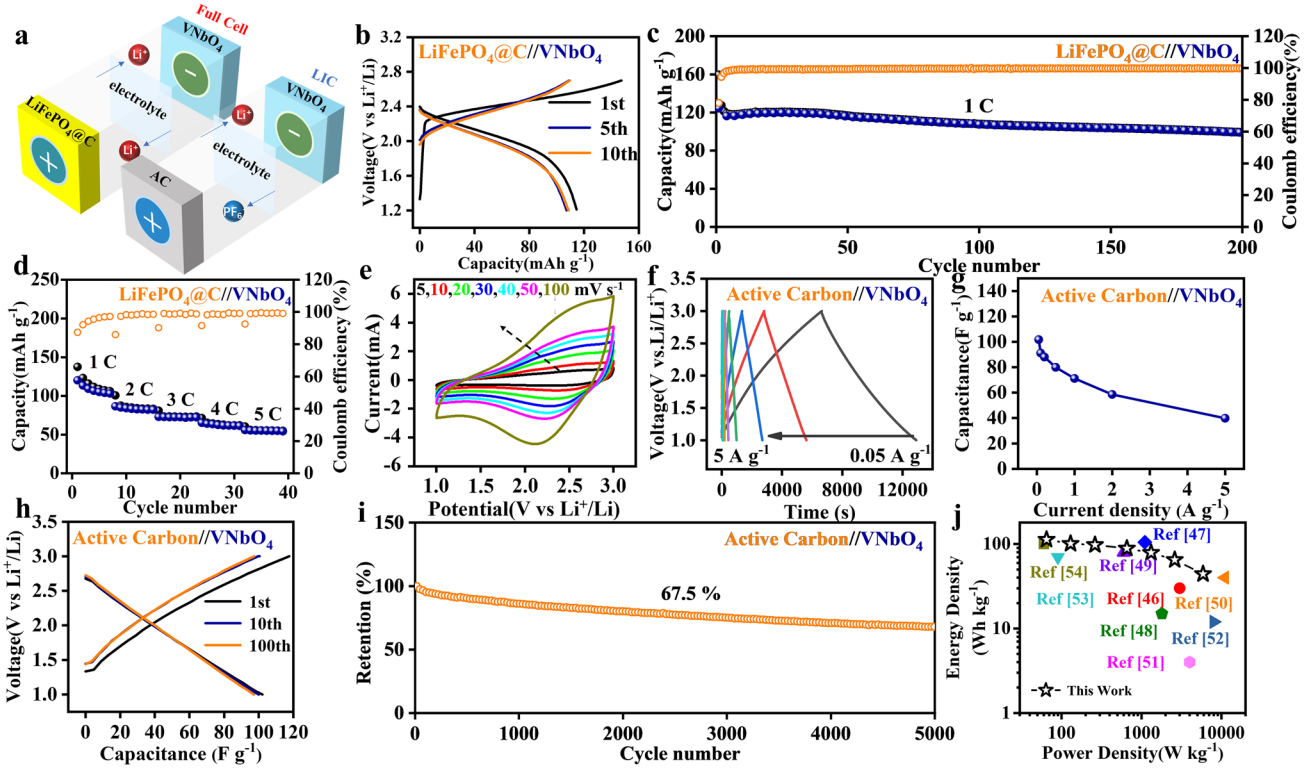

Fig. 6 **a** Models diagram of $LiFePO_4$@C//$VNbO_4$ full cell and AC//$VNbO_4$ LIC. **b** The selected charge/discharge profiles, **c** the cycle performance at 1C, **d** the rate performance of $LiFePO_4$@C//$VNbO_4$. **e** CV curves at different sweep rates (5–100 mV s^{-1}) and **f** the time-potential curves at different current densities of AC//$VNbO_4$. **g** Rate performance, **h** the selected charge/discharge profiles at 0.05 A g^{-1}, and **i** the cycle performance at 0.5 A g^{-1} of AC//$VNbO_4$. **j** The Ragone plot of AC//$VNbO_4$ compared with other reported niobium-based LICs

the stronger chemical affinity Li atoms and V atoms, the redox conversion of V^{3+}/V^{2+} couple has a higher priority than that of Nb^{4+}/Nb^{3+} in $VNbO_4$ anode during the lithiation/delithiation process. Therefore, the competitive redox strategy can effectively inhibit the over-reduction of Nb^{5+} to Nb^{3+} in $VNbO_4$, achieving a highly reversible redox chemistry in the long-term cycling processes. Besides, the spontaneous electron migration from V^{3+} to Nb^{5+} can greatly enhance the electronic conductivity $VNbO_4$ anode. As results, $VNbO_4$ electrode exhibits promising application potentials in both practical LIB and LIC devices, which indicates that competitive redox strategy provides a new idea for designing fast and durable anodes.

Acknowledgements We gratefully acknowledge the financial support from National Natural Science Foundation of China (51874142), Tip-top Scientific and Technical Innovative Youth Talents of Guangdong Special Support Program (2019TQ05L903) and Young Elite Scientists Sponsorship Program by CAST (2019QNRC001).

Funding Open access funding provided by Shanghai Jiao Tong University. Open access funding provided by South China University of Technology.

Declarations

Conflict of interest The authors declare no interest conflict. They have no known competing financial interests or personal relationships that could have appeared to influence the work reported in this paper.

Supplementary Information The online version contains supplementary material available at https://doi.org/10.1007/s40820-023-01172-9.

References

1. X. Zeng, M. Li, D. El-Hady, W. Alshitari, A. Al-Bogami et al., Commercialization of lithium battery technologies for electric vehicles. Adv. Energy Mater. **9**(27), 1900161 (2019). https://doi.org/10.1002/aenm.201900161
2. X. Ma, C. Ji, X. Li, Y. Liu, X. Xiong, Red@black phosphorus core-shell heterostructure with superior air stability for high-rate and durable sodium-ion battery. Mater. Today **59**, 36–45 (2022). https://doi.org/10.1016/j.mattod.2022.08.013
3. S. Lee, J. Kim, J. Moon, K. Jung, J. Kim et al., A cooperative biphasic MoO_x-MoP_x promoter enables a fast-charging lithium-ion battery. Nat. Commun. **12**(1), 39 (2021). https://doi.org/10.1038/s41467-020-20297-8
4. W. Cai, Y. Yao, G. Zhu, C. Yan, L. Jiang et al., A review on energy chemistry of fast-charging anodes. Chem. Soc. Rev. **49**(12), 3806–3833 (2020). https://doi.org/10.1039/c9cs00728h
5. X. Ding, Q. Huang, X. Xiong, Research and application of fast-charging graphite anodes for lithium-ion batteries. Acta Phys. Chim. Sin. **38**(11), 2204057 (2022). https://doi.org/10.3866/pku.Whxb202204057
6. Y. Rangom, T. Duignan, X. Zhao, Lithium-ion transport behavior in thin-film graphite electrodes with sei layers formed at different current densities. ACS Appl. Mater. Interfaces **13**(36), 42662–42669 (2021). https://doi.org/10.1021/acsami.1c09559
7. Z. Su, S. Li, L. Ma, T. Liu, M. Li et al., Quenching-induced defects liberate the latent reversible capacity of lithium titanate anode. Adv. Mater. **35**(5), 2208573 (2023). https://doi.org/10.1002/adma.202208573
8. M. Fan, Z. Lin, P. Zhang, X. Ma, K. Wu et al., Synergistic effect of nitrogen and sulfur dual-doping endows TiO_2 with exceptional sodium storage performance. Adv. Energy Mater. **11**(6), 2003037 (2021). https://doi.org/10.1002/aenm.202003037
9. Z. Hu, Q. He, Z. Liu, X. Liu, M. Qin et al., Facile formation of tetragonal-Nb_2O_5 microspheres for high-rate and stable lithium storage with high areal capacity. Sci. Bull. **65**(14), 1154–1162 (2020). https://doi.org/10.1016/j.scib.2020.04.011
10. X. Han, Q. Meng, X. Wan, B. Sun, Y. Zhang et al., Intercalation pseudocapacitive electrochemistry of Nb-based oxides for fast charging of lithium-ion batteries. Nano Energy **81**, 105635 (2021). https://doi.org/10.1016/j.nanoen.2020.105635
11. J. Meng, Q. He, L. Xu, X. Zhang, F. Liu et al., Identification of phase control of carbon-confined Nb_2O_5 nanoparticles toward high-performance lithium storage. Adv. Energy Mater. **9**(18), 1802695 (2019). https://doi.org/10.1002/aenm.201802695
12. D. Chen, J. Wang, T. Chou, B. Zhao, M. El-Sayed et al., Unraveling the nature of anomalously fast energy storage in T-Nb_2O_5. J. Am. Chem. Soc. **139**(20), 7071–7081 (2017). https://doi.org/10.1021/jacs.7b03141
13. Z. Song, H. Li, W. Liu, H. Zhang, J. Yan et al., Ultrafast and stable Li-(de) intercalation in a large single crystal H-Nb_2O_5 anode via optimizing the homogeneity of electron and ion transport. Adv. Mater. **32**(22), 2001001 (2020). https://doi.org/10.1002/adma.202001001
14. Y. Tang, L. Yang, Y. Zhu, F. Zhang, H. Zhang, Fabrication of a highly stable Nb_2O_5@C/CNTs based anolyte for lithium slurry flow batteries. J. Mater. Chem. A **10**(10), 5620–5630 (2022). https://doi.org/10.1039/d1ta10883b
15. Y. Chen, Z. Pu, Y. Liu, Y. Shen, S. Liu et al., Enhancing the low-temperature performance in lithium ion batteries of Nb_2O_5 by combination of W doping and mxene addition. J. Power Sources **515**, 230601 (2021). https://doi.org/10.1016/j.jpowsour.2021.230601
16. S. Shen, S. Zhang, X. Cao, S. Deng, G. Pan et al., Popcorn-like niobium oxide with cloned hierarchical architecture as advanced anode for solid-state lithium ion batteries. Energy Storage Mater. **25**, 695–701 (2020). https://doi.org/10.1016/j.ensm.2019.09.017
17. Q. Wang, Z. Jia, L. Li, J. Wang, G. Xu et al., Coupling niobia nanorods with a multicomponent carbon network for high power lithium-ion batteries. ACS Appl. Mater. Interfaces **11**(47), 44196–44203 (2019). https://doi.org/10.1021/acsami.9b14819
18. B. Deng, T. Lei, W. Zhu, L. Xiao, J. Liu, In-plane assembled orthorhombic Nb_2O_5 nanorod films with high-rate Li^+ intercalation for high-performance flexible Li-ion capacitors. Adv. Funct. Mater. **28**(1), 1704330 (2018). https://doi.org/10.1002/adfm.201704330
19. X. Ding, H. Huang, Q. Huang, B. Hu, X. Li et al., Doping sites modulation of T-Nb_2O_5 to achieve ultrafast lithium storage. J. Energy Chem. **77**, 280–289 (2023). https://doi.org/10.1016/j.jechem.2022.10.049
20. P. Jing, K. Liu, L. Soule, E. Wang, T. Li et al., Engineering the architecture and oxygen deficiency of T-Nb_2O_5-carbon-graphene composite for high-rate lithium-ion batteries. Nano Energy **89**, 106398 (2021). https://doi.org/10.1016/j.nanoen.2021.106398
21. F. Liu, X. Cheng, R. Xu, Y. Wu, Y. Jiang et al., Binding sulfur-doped Nb_2O_5 hollow nanospheres on sulfur-doped graphene networks for highly reversible sodium storage. Adv. Funct. Mater. **28**(18), 1800394 (2018). https://doi.org/10.1002/adfm.201800394
22. D. Luo, C. Ma, J. Hou, Z. Zhang, R. Feng et al., Integrating nanoreactor with O-Nb-C heterointerface design and defects engineering toward high-efficiency and longevous sodium ion battery. Adv. Energy Mater. **12**(18), 2103716 (2022). https://doi.org/10.1002/aenm.202103716
23. J. Lee, H. Kwak, S. Bak, G. Lee, S. Hong et al., New class of titanium niobium oxide for a Li-ion host: $TiNbO_4$ with purely single-phase lithium intercalation. Chem. Mater. **34**(2), 854–863 (2022). https://doi.org/10.1021/acs.chemmater.1c03960
24. L. Yan, J. Shu, C. Li, X. Cheng, H. Zhu et al., $W_3Nb_{14}O_{44}$ nanowires: ultrastable lithium storage anode materials for

advanced rechargeable batteries. Energy Storage Mater. **16**, 535–544 (2019). https://doi.org/10.1016/j.ensm.2018.09.008

25. L. Meng, R. Guo, F. Li, Y. Ma, J. Peng et al., Facile synthesis of flock-like V_2O_3/C with improved electrochemical performance as an anode material for Li-ion batteries. Energy Tech. **8**(3), 1900986 (2020). https://doi.org/10.1002/ente.201900986
26. S. Ni, J. Liu, D. Chao, L. Mai, Vanadate-based materials for Li-ion batteries: the search for anodes for practical applications. Adv. Energy Mater. **9**(14), 1803324 (2019). https://doi.org/10.1002/aenm.201803324
27. M. Yu, X. Bian, S. Liu, C. Yuan, Y. Yang et al., 3D hollow porous spherical architecture packed by iron-borate amorphous nanoparticles as high-performance anode for lithium-ion batteries. ACS Appl. Mater. Interfaces **11**(28), 25254–25263 (2019). https://doi.org/10.1021/acsami.9b06979
28. Y. Zhang, C. Kang, W. Zhao, B. Sun, X. Xiao et al., Crystallographic engineering to reduce diffusion barrier for enhanced intercalation pseudocapacitance of $TiNb_2O_7$ in fast-charging batteries. Energy Storage Mater. **47**, 178–186 (2022). https://doi.org/10.1016/j.ensm.2022.01.061
29. D. Liang, Y. Lu, L. Hu, L. Wang, S. Liang et al., Mesoporous $TiNb_2O_7$ nanosheets anode with excellent rate capability and cycling performance in lithium ion half/full batteries. J. Power Sourc. **544**, 231897 (2022). https://doi.org/10.1016/j.jpowsour.2022.231897
30. L. Xu, C. Thompson, Mechanisms of the cyclic (de)lithiation of RuO_2. J. Mater. Chem. A **8**(41), 21872–21881 (2020). https://doi.org/10.1039/d0ta06428a
31. L. Xu, C. Thompson, Electrochemically controlled reversible formation of organized channel arrays in nanoscale-thick RuO_2 films: Implications for mechanically stable thin films and microfluidic devices. ACS Appl. Nano Mater. **4**(12), 13700–13707 (2021). https://doi.org/10.1021/acsanm.1c03114
32. L. Xu, M. Chon, B. Mills, C. Thompson, Mechanical stress and morphology evolution in RuO_2 thin film electrodes during lithiation and delithiation. J. Power Sourc. **552**, 232260 (2022). https://doi.org/10.1016/j.jpowsour.2022.232260
33. X. Yan, T. Li, Y. Xiong, X. Ge, Synchronized ion and electron transfer in a blue T-Nb_2O_{5-x} with solid-solution-like process for fast and high volumetric charge storage. Energy Storage Mater. **36**, 213–221 (2021). https://doi.org/10.1016/j.ensm.2020.12.031
34. E. Lim, C. Jo, H. Kim, M. Kim, Y. Mun et al., Facile synthesis of Nb_2O_5@carbon core-shell nanocrystals with controlled crystalline structure for high-power anodes in hybrid supercapacitors. ACS Nano **9**(7), 7497–7505 (2015). https://doi.org/10.1021/acsnano.5b02601
35. R. Sahoo, T. Lee, D. Pham, T. Luu, Y. Lee, Fast-charging high-energy battery-supercapacitor hybrid: anodic reduced graphene oxide-vanadium (IV) oxide sheet-on-sheet heterostructure. ACS Nano **13**(9), 10776–10786 (2019). https://doi.org/10.1021/acsnano.9b05605
36. Y. Zheng, Z. Yao, Z. Shadike, M. Lei, J. Liu et al., Defect-concentration-mediated T-Nb_2O_5 anodes for durable and fast-charging Li-ion batteries. Adv. Funct. Mater. **32**(12), 2107060 (2022). https://doi.org/10.1002/adfm.202107060
37. S. Li, Q. Xu, E. Uchaker, X. Cao, G. Cao, Comparison of amorphous, pseudohexagonal and orthorhombic Nb_2O_5 for high-rate lithium ion insertion. CrystEngComm **18**(14), 2532–2540 (2016). https://doi.org/10.1039/c5ce02069g
38. F. Kong, L. Lv, J. Wang, G. Jiao, S. Tao et al., Graphite modified $AlNbO_4$ with enhanced lithium–ion storage behaviors and its electrochemical mechanism. Mater. Res. Bull. **97**, 405–410 (2018). https://doi.org/10.1016/j.materresbull.2017.09.034
39. X. Lou, R. Li, X. Zhu, L. Luo, Y. Chen et al., New anode material for lithium-ion batteries: aluminum niobate ($AlNb_{11}O_{29}$). ACS Appl. Mater. Interfaces **11**(6), 6089–6096 (2019). https://doi.org/10.1021/acsami.8b20246
40. X. Cai, H. Yan, R. Zheng, H. Yu, Z. Yang et al., $Cu_2Nb_{34}O_{87}$ nanowires as a superior lithium storage host in advanced rechargeable batteries. Inorg. Chem. Front. **8**(2), 444–451 (2021). https://doi.org/10.1039/d0qi01075h
41. T. Wang, T. Ge, S. Shi, M. Wu, G. Yang, Synthesis of wolframite $FeNbO_4$ nanorods as a novel anode material for improved lithium storage capability. J. Alloys Compd. **740**, 7–15 (2018). https://doi.org/10.1016/j.jallcom.2017.12.369
42. L. Yan, H. Lan, H. Yu, S. Qian, X. Cheng et al., Electrospun $WNb_{12}O_{33}$ nanowires: superior lithium storage capability and their working mechanism. J. Mater. Chem. A **5**(19), 8972–8980 (2017). https://doi.org/10.1039/c7ta01784g
43. H. Yu, X. Cheng, H. Zhu, R. Zheng, T. Liu et al., Deep insights into kinetics and structural evolution of nitrogen-doped carbon coated $TiNb_{24}O_{62}$ nanowires as high-performance lithium container. Nano Energy **54**, 227–237 (2018). https://doi.org/10.1016/j.nanoen.2018.10.025
44. Y. Yuan, H. Yu, X. Cheng, R. Zheng, T. Liu et al., Preparation of $TiNb_6O_{17}$ nanospheres as high-performance anode candidates for lithium-ion storage. Chem. Eng. J. **374**, 937–946 (2019). https://doi.org/10.1016/j.cej.2019.05.225
45. S. Qian, H. Yu, L. Yang, H. Zhu, X. Cheng et al., High-rate long-life pored nanoribbon VNb_9O_{25} built by interconnected ultrafine nanoparticles as anode for lithium-ion batteries. ACS Appl. Mater. Interfaces **9**(36), 30608–30616 (2017). https://doi.org/10.1021/acsami.7b07460
46. G. Tang, L. Cao, P. Xiao, Y. Zhang, H. Liu, A novel high energy hybrid Li-ion capacitor with a three-dimensional hierarchical ternary nanostructure of hydrogen-treated TiO_2 nanoparticles/conductive polymer/carbon nanotubes anode and an activated carbon cathode. J. Power Sourc. **355**, 1–7 (2017). https://doi.org/10.1016/j.jpowsour.2017.04.053
47. L. Chen, D. Tsai, J. Chen, Phenylphenol-derived carbon and antimony-coated carbon nanotubes as the electroactive materials of lithium–ion hybrid capacitors. ACS Appl. Mater. Interfaces **11**(38), 34948–34956 (2019). https://doi.org/10.1021/acsami.9b10579
48. Q. Wang, Z. Wen, J. Li, A hybrid supercapacitor fabricated with a carbon nanotube cathode and a TiO_2-B nanowire anode. Adv. Funct. Mater. **16**(16), 2141–2146 (2006). https://doi.org/10.1002/adfm.200500937

49. H. Wang, C. Guan, X. Wang, H. Fan, A high energy and power Li–ion capacitor based on a TiO_2 nanobelt array anode and a graphene hydrogel cathode. Small **11**(12), 1470–1477 (2015). https://doi.org/10.1002/smll.201402620
50. R. Bi, N. Xu, H. Ren, N. Yang, Y. Sun et al., A hollow multi-shelled structure for charge transport and active sites in lithium-ion capacitors. Angew. Chem. Int. Ed. **59**(12), 4865–4868 (2020). https://doi.org/10.1002/anie.201914680
51. X. Wang, L. Ge, C. Zheng, V. Augustyn, X. Ma et al., High-performance supercapacitors based on nanocomposites of Nb_2O_5 nanocrystals and carbon nanotubes. Adv. Energy Mater. **1**(6), 1089–1093 (2011). https://doi.org/10.1002/aenm.201100332
52. W. Xu, C. Yan, Y. Jian, A. Sumboja, P. Lee et al., Orthorhombic niobium oxide nanowires for next generation hybrid supercapacitor device. Nano Energy **11**, 765–772 (2015). https://doi.org/10.1016/j.nanoen.2014.11.020
53. L. Kong, C. Zhang, J. Wang, W. Qiao, L. Ling, Free-standing T-Nb_2O_5/graphene composite papers with ultrahigh gravimetric/volumetric capacitance for Li–ion intercalation pseudocapacitor. ACS Nano **9**(11), 11200–11208 (2015). https://doi.org/10.1021/acsnano.5b04737
54. S. Li, T. Wang, W. Zhu, J. Lian, Y. Huang et al., Controllable synthesis of uniform mesoporous H-Nb_2O_5/rGO nanocomposites for advanced lithium ion hybrid supercapacitors. J. Mater. Chem. A **7**(2), 693–703 (2019). https://doi.org/10.1039/c8ta10239b

 https://doi.org/10.1007/s40820-023-01172-9